Atmos. Chem. Phys. Discuss., 12, 25983–26028, 2012
www.atmos-chem-phys-discuss.net/12/25983/2012/
doi:10.5194/acpd-12-25983-2012

Atmospheric Chemistry and Physics Discussions

Aerosol classification by airborne high spectral resolution lidar observations

S. Groß[1], M. Esselborn[1,*], B. Weinzierl[1], M. Wirth[1], A. Fix[1], and A. Petzold[1,]**

[1]Institut für Physik der Atmosphäre, Deutsches Zentrum für Luft- und Raumfahrt (DLR), Oberpfaffenhofen, 82234 Weßling, Germany
[*]now at: European Southern Observatory, Karl-Schwarzschild-Str. 2, 85748 Garching, Germany
[**]now at: Institut für Energie- und Klimaforschung IEK-8: Troposphäre, Forschungszentrum Jülich GmbH, 52425 Jülich, Germany

Received: 8 August 2012 – Accepted: 20 September 2012 – Published: 2 October 2012

Correspondence to: S. Groß (silke.gross@dlr.de)

Published by Copernicus Publications on behalf of the European Geosciences Union.

Abstract

During four aircraft field experiments with the DLR research aircraft Falcon in 1998 (LACE), 2006 (SAMUM-1) and 2008 (SAMUM-2 and EUCAARI), airborne High Spectral Resolution Lidar (HSRL) and in situ measurements of aerosol microphysical and optical properties were performed. Altogether, the properties of six different aerosol types and aerosol mixtures – Saharan mineral dust, Saharan dust mixtures, Canadian biomass burning aerosol, African biomass burning aerosol, anthropogenic pollution aerosol, and marine aerosol have been studied. On the basis of this extensive HSRL data set, we present an aerosol classification scheme which is also capable to identify mixtures of different aerosol types. We calculated mixing lines that allowed us to determine the contributing aerosol types. The aerosol classification scheme was validated with in-situ measurements and backward trajectory analyses. Our results demonstrate that the developed aerosol mask is capable to identify complex stratifications with different aerosol types throughout the atmosphere.

1 Introduction

Aerosol particles affect both directly and indirectly the Earth's climate system by scattering solar and terrestrial radiation and by influencing the properties of clouds. In contrast to long-lived greenhouse gases the climate effects of short-lived aerosol particles differ strongly on regional and temporal scales. Currently, the magnitude of the (anthropogenic) aerosol impact on climate causes the largest uncertainty in our knowledge on climate change (IPCC, 2007). Considerable uncertainties in quantifying the global direct radiative effects of aerosols arise from the variability of the spatial distribution of aerosols as well as from uncertainties associated with aerosol optical and microphysical properties, which vary as a function of aerosol age and type. Reducing these uncertainties requires routine aerosol observations with high vertical and horizontal resolution. Airborne measurements are an appropriate tool for aerosol studies, as they

ACPD
12, 25983–26028, 2012

provide highly resolved datasets, but lack in the spatial and temporal coverage of the Earth. Spaceborne lidar systems provide measurements of aerosol layers on a global scale, so they have the potential to advance our knowledge about this important component of the climate system tremendously. However, methods to distinguish different aerosol types and validations of these methods are essential. For example, the Cloud-Aerosol Lidar and Pathfinder Satellite Observations (CALIPSO) mission launched in 2006 (Winker et al., 2007) has completed its fifth year of successful in-orbit operation. Designed as an elastic-backscatter lidar it detects attenuated atmospheric backscatter but lacks the ability of extinction measurements. In order to derive aerosol extinction from the lidar backscatter signals the aerosol's extinction-to-backscatter ratio, also commonly referred to as the aerosol lidar ratio S_p has to be assumed. There is no standardized value of S_p. It rather depends on the particles' microphysical and chemical properties and therefore varies significantly for different aerosol types. Recent studies have shown that typical lidar ratios at 532 nm are 18 ± 5 sr for marine aerosol (Groß et al., 2011a), 56 ± 5 sr for desert dust (Tesche et al., 2009a), and 60 ± 12 sr for arctic haze (Müller et al., 2007). Lidar ratio assumptions for a specific scene not supported by additional information consequently result in doubtful extinction data. Sophisticated aerosol classification algorithms and lidar ratio selection schemes have been developed to help linking the aerosol observations with appropriate lidar ratios (Omar et al., 2009; Müller et al., 2011). However, even if the aerosol type is perfectly identified, the retrieved extinction is subject to the input value of the associated aerosol type's lidar ratio, as is shown e.g. by Wandinger et al. (2010).

Next-generation spaceborne lidars are designed as high spectral resolution lidars (HSRL) (Ingmann, 2004; Petzold et al., 2011). Like Raman lidar systems (Ansmann et al., 1990) the HSRL enables direct measurements of aerosol extinction profiles without assumptions of a lidar ratio (Shipley et al., 1983; Shimizu et al., 1983; Hair et al., 2008; Esselborn et al., 2008). Two future satellite missions of the European Space Agency (ESA) will deploy HSRL systems. The ALADIN (Atmospheric LAser Doppler INstrument) instrument (Reitebuch et al., 2009) will be the key instrument of the ESA

ACPD
12, 25983–26028, 2012

Atmospheric Dynamics Mission (ADM) and is expected for launch in 2015. It is designed as an incoherent Doppler wind lidar at 355 nm and is expected to also have potential for extinction profiling (Ansmann et al., 2007). The ATLID (ATmospheric LIDar) instrument will be part of the Earth Clouds, Aerosols and Radiation Explorer (EarthCARE) mission (ESA, 2004) aiming for satellite launch in 2015. Measuring at 355 nm, ATLID is expected to provide aerosol and cloud optical properties and, in synergy with other active and passive instruments on board of EarthCARE, collocated samples of the state of the atmosphere along the satellite track.

In this study we show the great potential of combined HSRL and depolarization measurements in a similar way as recently done by Burton et al. (2012). We provide aerosol lidar ratio S_p, particle linear depolarization ratio δ_p, and color ratio CR of various aerosol types measured with HSRL at 532 nm. Our measurements were performed over Europe, the Saharan desert and the Cape Verde Islands and therewith extend the database presented by Burton et al. (2012) especially with respect to fresh Saharan dust collected near the source regions. Furthermore we present a method to calculate S_p and δ_p for aerosol mixtures, which is crucial to differentiate mixtures from pure aerosol types, and to determine the contributing aerosol types to the mixture. In addition, our findings are supported by trajectory analysis and validated with in-situ measurements. In addition, this study demonstrates that different aerosol types can be distinguished using aerosol lidar ratio and particle linear depolarization ratio even if only one HSRL wavelength is available, as it will be the case for the EarthCARE mission.

2 Methods

2.1 Data basis

During four field campaigns aerosol properties have been measured by airborne high spectral resolution lidar onboard the DLR Falcon research aircraft and an extensive set

ACPD
12, 25983–26028, 2012

of aerosol in-situ instruments. The comprehensive data sets obtained throughout these field experiments contain information on some of the most prominent atmospheric aerosol types: Mineral dust aerosol, sea salt aerosol, biomass burning aerosol, and anthropogenic pollution aerosol. In the following we briefly describe the four field experiments.

- LACE98: The Lindenberg Aerosol Characterization Experiment, Germany, 1998 (Ansmann et al., 1998) took place in July/August 1998 at the Lindenberg Meteorological Observatory of the German Weather Service (52.2° N, 14.1° E) located 70 km southeast of Berlin/Germany. LACE98 was carried out as a column closure study (Quinn et al., 1996) with the goal of providing experimental data on the vertical and temporal variability of microphysical and optical aerosol properties measured at a continental European site. Two research aircraft were deployed to probe the aerosol column over the instrumented ground station at Lindenberg: the piston-engine powered Partenavia aircraft carried in-situ instrumentation and probed mainly the boundary layer whereas the turbofan powered DLR Falcon aircraft was equipped with HSRL, radiation and aerosol in-situ instruments and performed flights in the upper troposphere and stacked in-situ profiles across the tropospheric column over the ground site. LACE98 contributes cases of anthropogenically influenced boundary layer aerosol and Canadian forest fire aerosols from a long-range transport event (Petzold et al., 2002).

- SAMUM-1: The Saharan Mineral Dust Experiment, Morocco, 2006 (Heintzenberg, 2009) took place in May/June 2006 and aimed at the characterization of physical, chemical and radiative properties of African mineral dust. The field experiment involved two instrumented ground stations in Southern Morocco: Ouarzazate (30.9° N, 6.9° W) and Tinfou, which is located about 30 km southeast of Zagora (30.3° N, 5.8° W). Similar to LACE98 the Partenavia aircraft and the Falcon aircraft were deployed during SAMUM-1. A total of 17 Falcon research flights were carried out. Ground-based and airborne observations were coordinated with overpasses

ACPD
12, 25983–26028, 2012

of MISR (multi-angle imaging spectroradiometer) on NASA's Aqua satellite, and MERIS (medium resolution imaging spectrometer) on ESA's ENVISAT satellite as well (Kahn et al., 2009; Dinter et al., 2009). In this respect SAMUM-1 was among the first studies to combine collocated and coordinated ground-based, airborne and satellite measurements of aerosols.

– SAMUM-2: The Saharan Mineral Dust Experiment, Cape Verde Islands, 2008 (Ansmann et al., 2011) took place in January/February 2008 and focused on the observation of aged Saharan dust and mixtures of Saharan dust with biomass burning aerosol from the African tropical regions and marine aerosols. Praia (14.9° N, 23.5° W) the capital of Santiago/Cape Verde was chosen for the ground-based lidar and in-situ measurements. Altogether, the DLR Falcon performed 17 research flights in the well stratified troposphere. Lidar cases of marine boundary layer aerosol were also collected during SAMUM-2, while respective particle number size distributions were taken from focused studies in the North Atlantic region which, however, where conducted without HSRL deployment (Petzold et al., 2008).

– EUCAARI-LONGREX: The European integrated project on Aerosol Cloud Climate and Air Quality Interactions, Long-range experiment, 2008 (Kulmala et al., 2009) investigated the physical and chemical properties of aerosols on a European scale, involving 48 partners from 25 countries. In May/June 2008 the DLR Falcon research aircraft performed 14 flight missions (Hamburger et al., 2011). Ground-based measurement activities were carried out at a number of research sites.

The main measurement areas for this study are shown in Fig. 1. Detailed information to the analyzed case studies can be found in Table 1.

ACPD
12, 25983–26028, 2012

2.2 The DLR high spectral resolution lidar

The first airborne HSRL system designed and built by DLR and operated during LACE98, is described in Wandinger et al. (2002). Since then the system was under further development. A detailed technical description of the HSRL system deployed during SAMUM-1 and a presentation of its measurements can be found in Esselborn et al. (2008) and Esselborn et al. (2009). The most advanced system was deployed during SAMUM-2 and EUCAARI-LONGREX. The system, also known as WALES (Water vapor Lidar Experiment in Space) has been primarily designed as an airborne high-performance multi-wavelength differential absorption lidar (DIAL) for water vapor measurements at 935 nm but additionally provides a HSRL-channel at 532 nm and depolarization channels at 1064 nm and 532 nm for aerosol characterization (Wirth et al., 2009). The lidar system utilizes two identical high-power, Q-switched, single-longitudinal-mode Nd : YAG lasers, each of them providing a pulse energy of 400 mJ at 1064 nm at a repetition rate of 100 Hz. The fundamental output of each laser is firstly frequency-doubled to 532 nm and then converted to 935 nm by an optical parametric oscillator (OPO). The lasers are frequency stabilized to an iodine absorption line. The OPO of both laser systems can be switched on and off, depending on whether water vapor at 935 nm should be measured or all the power at 532 nm should be used for the HSRL measurement at 532 nm. During EUCAARI-LONGREX one of the laser systems was used for water vapor measurement and the other was used for HSRL measurements. The backscattered light is collected using a lightweight Cassegrain telescope with an aperture diameter of 0.48 m and a focal length of 5 m. The field of view of all channels is 1.6 mrad. Dichroic beamsplitters are used to spectrally separate the backscatter signals at the three wavelengths. Polarization beamsplitter cubes separate the parallel- and cross-polarized components of the backscattered light at 532 nm and 1064 nm.

ACPD
12, 25983–26028, 2012

2.3 In-situ instrumentation

Besides the HSRL system, the Falcon was equipped with a variety of in-situ instruments during all campaigns. The in-situ payload consisted of different aerosol sizing instruments, which covered the particle size range from 4 nm to 100 µm in diameter. Instruments sensitive to the sub-µm fraction such as condensation particle counters (CPC) for measuring the particle number concentration and differential mobility analyzers (DMA) were operated inside the aircraft cabin whereas optical sizing instruments covering the size range up to 100 µm in diameter were operated outside the fuselage of the Falcon at wing stations. The optical particle spectrometers used during the studies were a Passive Cavity Aerosol Spectrometer Probe (PCASP-100X; $0.12 < D_p < 3.5$ µm) and two Forward Scattering Spectrometer Probes (FSSP 300: $0.3 < D_p < 30$ µm; FSSP 100: $1.0 < D_p < 100$ µm). Detailed descriptions of the particle-sizing instrumentation are given by Petzold et al. (2002) and Weinzierl et al. (2009, 2011).

Aerosol absorption was measured inside the cabin at wavelengths 467, 530 and 660 nm by means of a three-wavelength particle soot absorption photometer (PSAP). More detail on the absorption measurements are shown in Petzold et al. (2009, 2011). The absorption Angström exponent å characterizes the wavelength-dependence of the aerosol absorption coefficient in terms of a power law $\lambda^{-å}$. This property has characteristic values for different types of light-absorbing aerosols. It approaches unity for combustion-derived soot particles in anthropogenically polluted air masses and may exceed a value of 3 for mineral dust. During SAMUM-1 and SAMUM-2 typical values of 3.1–5.0 were found for Saharan dust (Petzold et al., 2009; Weinzierl et al., 2011). For African biomass burning aerosol a median value of 1.34 was found (Weinzierl et al., 2011).

2.4 Measurement strategy

During all campaigns the DLR HSRL was operated aboard the Falcon research aircraft together with the set of in-situ probing instruments. The HSRL measured aerosol

ACPD
12, 25983–26028, 2012

optical quantities at $\lambda = 532$ nm namely the aerosol backscatter coefficient, aerosol extinction coefficient, aerosol optical depth, the aerosol lidar ratio and particle linear depolarization ratio. By means of coordinated in-situ soundings, measurements of aerosol number concentration, aerosol number size distribution, and aerosol absorption coefficient have been performed. The sampling strategy during the field experiments generally consisted of two parts: First, remote HSRL sounding was performed at high altitudes to observe and identify interesting aerosol layers. Subsequently, the aerosol layers identified by the HSRL were probed with the in-situ instruments at several different flight altitudes (Fig. 2).

2.5 Backward trajectories

To locate possible aerosol source regions, backward trajectories and satellite images were used. The trajectories were calculated with the Hybrid Single Particle Lagrangian Integrated Trajectory (HYSPLIT) model (Draxler and Rolph, 2012) and the NCEP Global Data Assimilation System (GDAS) data. For LACE98 NCEP Reanalysis data were used. We compared the temporally resolved backward trajectories with information of fire burning times (e.g. MODIS Burnt Area Product), of dust release periods (e.g. Meteosat Second Generation (MSG) dust RGB composite images), and of air pollution, considering the HYSPLIT local mixing layer heights and the trajectories heights, to assess the aerosol source regions of the examined air masses. Uncertainties in this approach, caused by unresolved vertical mixing processes, and by general uncertainties of the trajectory calculations are estimated to be in the range of 15–20 % of the trajectory distance (Stohl et al., 2002). Trajectory calculations with slightly modified initial conditions with respect to the arrival time, location and altitude may check their reliability.

Figure 3 shows back trajectories for the different aerosol types observed during LACE98, SAMUM-1, SAMUM-2 and EURCAARI-LONGREX. The trajectories are color-coded with respect to distinct aerosol types, representing the aerosol layers identified by the lidar measurements. According to the respective prevailing synoptic

ACPD
12, 25983–26028, 2012

situation, the trajectories show different flow patterns and source regions for the different campaigns. The source region of the dust loaded air masses during SAMUM-1 and SAMUM-2 are clearly located in the Saharan desert as is obvious from panel (a) and (b). In contrast, the air masses corresponding to African biomass burning aerosols (c) originate from the Central African region and the Gulf of Guinea. During this time of the year most of the forest and grassland fires are located in this area as can be seen from satellite data, e.g. the MODIS fire maps (http://rapidfire.sci.gsfc.nasa.gov/firemaps/), not shown here. Within the marine boundary layer (d) there is no influence of the Saharan desert and African fires. Trajectories for the EUCAARI-LONGREX campaign (e) show a circulating flow pattern over Europe, due to an anti-cyclonic blocking event over Central Europe that led to an increase of pollution concentration within the boundary layer. Air masses observed during LACE98 (f) originated from Canada, where a lot of forest fires were detected at that time.

3 Results

3.1 Vertical layering

Figure 4 presents the typical stratification for each of the four field experiments. All panels of Fig. 4 show the backscatter ratio BSR = β/β_a (with β the total backscatter coefficient and β_a the aerosol backscatter coefficient) measured at 532 nm with the HSRL system. Differences in the aerosol load and vertical structure during the different field experiments are obvious. LACE98 (Fig. 4, upper left panel) was characterized by a shallow boundary layer of less than 1 km thickness, and an elevated layer between 3–5 km containing Canadian biomass burning aerosols. The structure of the biomass burning layer was very inhomogeneous. During EUCAARI-LONGREX the anthropogenic pollution aerosol was mainly confined to the boundary layer which extended up to an altitude of about 3 km, and a thin elevated aerosol layer in about 3.5 km above ground. Convective clouds developed at the boundary layer top (white areas).

ACPD
12, 25983–26028, 2012

During SAMUM-1 the Saharan mineral dust aerosol was concentrated in the well-mixed boundary layer and extended from the ground up about 6 km a.s.l. In contrast to the first campaign, the atmosphere during SAMUM-2 showed a complex multi-layer structure with a shallow boundary layer of about 0.5 km extent often topped by a second layer reaching up to 1.5 km a.s.l. and an elevated layer in 2–5 km a.s.l.

3.2 Aerosol type identification

As we have shown in the previous section, often different aerosol types are present at different altitudes throughout the atmosphere. Therefore column-integrated measurements at the ground are not sufficient for an aerosol type classification and also for the derivation of aerosol microphysical and optical properties. Either airborne in-situ measurements or a classification scheme based on remote sensing techniques are mandatory. We now present a method for aerosol type classification which uses advanced lidar measurements.

Based on the HSRL measurements, two aerosol specific quantities, so called intensive quantities, the aerosol lidar ratio and the particle linear depolarization ratio δ_p, are derived. Furthermore, the color ratio CR (ratio of aerosol backscatter coefficient at 532 nm and 1064 nm) is calculated. Past analyses of these quantities reveal that characteristic values can be attributed to the different aerosol types (Tesche et al., 2009b, 2011; Groß et al., 2011a, 2012, Weinzierl et al., 2011, Burton et al., 2012).

Figure 5 shows measurements of the three intensive aerosol quantities, S_p versus δ_p (a), δ_p versus CR (b), and CR versus S_p (c), as well as the frequency distribution of these intensive quantities (d–f). Different clusters of data pairs can be identified in panels (a–c). It is obvious that δ_p shows the largest differences for the different aerosol types (Fig. 5a, d). The spread ranges from low δ_p values for marine aerosols of 1–11 % (mean value: 3 ± 1 %) to high δ_p values of 25–43 % (mean value: 32 ± 2 %) for fresh Saharan dust. Values of δ_p of 21–31 % (mean value: 27 ± 2 %) were also found in mixed Saharan dust layers while δ_p of 8–26 % (mean value: 14 ± 2 %) were found for African biomass burning aerosol mixtures (Weinzierl et al., 2011, Tesche et al.,

ACPD
12, 25983–26028, 2012

2009b). Although some (pure) aerosol types are clearly distinguishable by their particle linear depolarization ratio, this parameter fails to differentiate marine aerosols and anthropogenic pollution aerosols or aged (Canadian) biomass burning aerosols. These three aerosol types show quite similar δ_p values, but differ strongly in color and lidar ratio (Fig. 5c, f). While S_p for marine aerosols is low with a mean value of 18 ± 5 sr (0–33 sr), anthropogenic pollution aerosols show a significantly higher mean value of 56 ± 6 sr (33–72 sr). A similar mean lidar ratio was found for fresh Saharan dust and mixed Saharan dust of 48 ± 5 sr (33–68 sr) and 50 ± 4 sr (32–71 sr), respectively. For African biomass burning aerosol a mean value of 63 ± 7 sr (36–91 sr) was found. The mean value of Canadian biomass burning aerosols is even higher with 69 ± 17 sr. However, as the aerosol concentration in the Canadian biomass burning layers was very low, the uncertainties in the retrieved intensive aerosol quantities for this aerosol type are large. While δ_p and S_p show quite different values for the different aerosol types, CR (Fig. 5b, e) is similar for the different types of aerosols, except anthropogenic pollution aerosols and Canadian biomass burning aerosols. Canadian biomass burning aerosols show a wide spread of CR from 1.4 to 16.2 (mean value: 4.70 ± 1.30), but as mentioned before, the uncertainties are large. For anthropogenic pollution aerosols values range between 1.72 and 3.45 (mean value: 2.43 ± 0.27). All other examined aerosol types show values of 1.04–2.41 with similar mean values of 1.30 ± 0.15 for fresh Saharan dust, 1.48 ± 0.09 for mixed Saharan dust, 1.63 ± 0.13 for African biomass burning aerosols, and 1.64 ± 0.10 for marine aerosols. These examples show that only the combination of different aerosol quantities permits a meaningful discrimination of aerosol types. The mean values of δ_p, S_p and CR, as well as their range, value of maximum frequency and median are listed in Table 2.

To determine the frequency distribution the sample space was subdivided in bins of 0.1 % in case of the particle linear depolarization ratio, of 0.5 sr in case of the lidar ratio, and of 0.01 in case of the color ratio of backscatter. As can be seen from Fig. 5 the frequency distribution of the color ratio of the backscatter coefficient is quite narrow for most of the particle types (Fig. 5e); except for Canadian biomass burning

ACPD
12, 25983–26028, 2012

aerosols (see discussion above). Looking at the particle linear depolarization ratio the frequency distribution for the different aerosol types looks different (Fig. 5d). While the frequency distribution shows one main peak for anthropogenic pollution aerosol and Saharan dust, two or more peaks exist for African biomass burning mixtures and mixed Saharan dust. For marine aerosols a broadening towards higher values is obvious. The latter may be caused by mixing of various amounts of the contributing aerosol types. Although the effect is not as distinctive for the lidar ratio (Fig. 5f) a small second peak at the frequency distribution of the African biomass burning aerosols and the broadening towards higher values for marine aerosols are still visible. As a result, the mean value, the value of maximum frequency and the median of these aerosol types show the highest differences (see Table 2).

3.3 Aerosol mixtures

In nature not only "pure" dust, biomass burning, or marine aerosols are observed, but also mixtures of different aerosol types. Now the question is whether these aerosol mixtures can be identified and whether the fraction of the individual aerosol types can be determined on the basis of δ_p and S_p. Figure 6 shows the $S_p - \delta_p$ – space. The solid lines in Fig. 6 depict mixing lines for different aerosol types (marine aerosols and Saharan dust – Fig. 6, thin lines; (Canadian) biomass burning aerosols and Saharan dust – Fig. 6, thick lines) based on Formulas 5 and 6 in Groß et al. (2011a) using the S_p and δ_p values of the pure aerosol types to calculate S_p and δ_p of the mixture. The values of S_p and δ_p for selected mixing ratios of marine aerosol and Saharan dust mixtures, and Canadian (aged) biomass burning aerosol and Saharan dust mixtures are listed in Table 3.

The second feature visible in Fig. 6 is that the values for the African biomass burning aerosol cluster (Fig. 6, green dots) are clearly located within the mixing lines of Saharan dust and Canadian biomass burning aerosols. This is in agreement with findings of the SAMUM-2 campaign, where they found a contribution of different amount of Saharan dust within these aerosol layers (Lieke et al., 2011; Weinzierl et al., 2011). Besides the

ACPD
12, 25983–26028, 2012

African biomass burning aerosol cluster, also the mixed Saharan dust cluster (Fig. 6, red dots) is within the mixing lines. The differentiation of mixtures of Saharan dust and marine aerosols, and Saharan dust and biomass burning aerosols is difficult as soon as Saharan dust contributes significantly to that mixture. In this case further information like trajectory analysis is crucial. During SAMUM-2 a Saharan dust contribution of approximately 10–40 % in the marine aerosol dominated boundary layer was found, and of 85–98 % when the boundary layer was dominated by Saharan dust (Groß et al., 2011b). In the mixed Saharan dust layer the contribution of Saharan dust was about 85–95 % with small contribution of biomass burning aerosols (Weinzierl et al., 2011).

3.4 Microphysical properties

Figure 7 summarizes particle number size distributions of identified aerosol types. The distinct properties of identified aerosol types can be directly linked to respective intensive aerosol quantities determined by lidar as will be discussed in the following. In general terms, the lidar ratio S_p is sensitive to the particle size and to the absorption properties: S_p decreases with increasing particle size and increases with increasing light absorption.

In the presented cases all combustion aerosols (anthropogenic pollution, Canadian boreal forest fire, African biomass burning) are characterised by strong light absorption in the visible spectral range and by an absorption Angström exponent of 1–2. Real parts of the complex refractive index of the particles are mostly > 1.5, and imaginary parts vary from 0.01i to 0.07i for 532 nm (Wandinger et al., 2002; Petzold et al., 2007; Weinzierl et al., 2011).

Respective lidar ratios vary from less than 60 sr to 68 sr. Values are highest compared to all observed aerosol types and do not differ significantly among combustion-derived aerosol types. Both Canadian boreal forest fire aerosol and African biomass burning aerosol from Savannah fires are characterized by a dominant accumulation mode which peaks between 200 and 300 nm in diameter. While Canadian forest fire aerosol particles are mainly smaller than 1 µm in diameter, the Savannah fire aerosol

ACPD
12, 25983–26028, 2012

contains a considerable fraction of super-µm sized particles originating from areas with strong dust emissions further north where the airmasses had passed prior to entering the Savannah fire region. The significant difference in the particle linear depolarization ratio between less than 10 % for Canadian fire aerosols and 14 ± 2 % for African biomass burning aerosols can be attributed to the super-µm sized dust particles (see Fig. 6). The even lower value of δ_p for anthropogenic pollution aerosol may be associated to the fact that anthropogenic pollution is dominated by an Aitken mode aerosol with its modal diameter well below 100 nm and an accumulation mode significantly smaller than the accumulation mode for aged biomass burning aerosols of various origins (Petzold et al., 2002; Hamburger et al., 2012).

Besides combustion-derived particles, mineral dust is the other major light-absorbing component of the atmospheric aerosol. However, its ability for light absorption is much weaker than that of carbonaceous combustion particles. Respective refractive index values at 532 nm are 1.55–1.57 for the real part and 1×10^{-3} to 8×10^{-3} for the imaginary part (Petzold et al., 2009; Weinzierl et al., 2011). Consequently, pure and mixed mineral dust also show high values of the lidar ratio S_p, however at the bottom end of values covered by carbonaceous particles. The significant difference in δ_p between combustion particles and mineral dust is attributed solely to the dominating fraction of irregularly shaped dust particles in the super-µm size range with its modal diameter at 5–10 µm.

Marine aerosol also has a significant component of super-µm sized sea salt particles. However, since these particles are very likely spherically shaped due to the high relative humidity in the marine boundary layer and the hygroscopic nature of sea salt, the resulting particle linear depolarization ratio is small. Furthermore, sea salt aerosol is mainly non-absorbing with a vanishing imaginary part of the refractive index so that the resulting lidar ratio is small.

In summary, we find that the observed pattern of aerosol optical properties derived from lidar measurements can be linked phenomenologically to their intensive microphysical and optical properties.

ACPD
12, 25983–26028, 2012

4 Discussion

4.1 Comparison with former studies

4.1.1 Saharan dust

The investigation of optical properties of mineral dust is a major topic in atmospheric research. Therefore a number of publications address this subject. At this point only a brief synopsis of the main key findings concerning the examined lidar derived intensive optical properties will be given. Reported are lidar ratios in the range of about 40–70 sr and a mean particle linear depolarization ratio of about 31 % (Table 4). Considering the lidar ratio, the mean values found for pure Saharan dust during the SAMUM-2 winter campaign are slightly higher than those of SAMUM-1 (and other field experiments). However, during the SAMUM-2 winter campaign higher iron content was found in the Saharan dust layer (Kandler et al., 2011; Müller et al., 2011) compared to SAMUM-1. The increase in the iron content affects the absorption properties of the aerosols and may explain the slightly higher values found during SAMUM-2. The changes can be attributed to possible differences in the main dust source region of SAMUM-1 and SAMUM-2 (winter) or to aging of the dust particles during transport (see Weinzierl et al., 2011). Our values for the lidar ratio and the particle linear depolarization ratio at 532 nm for pure Saharan dust are in very good agreement with these findings.

4.1.2 Mixed Saharan dust

A summary of δ_p and S_p found from ground-based lidar measurements for mixed Saharan dust layers can be found in Table 5. Comparing these results, it has to be kept in mind that the values for the lidar ratio and the particle linear depolarization ratio of dust mixtures strongly depend on the amount of dust in the mixture, and on the kind of mixture, i.e. the contributing aerosol types.

ACPD
12, 25983–26028, 2012

4.1.3 Biomass burning aerosols (fresh/aged), and anthropogenic pollution

Information of δ_p and S_p found in fresh or aged biomass burning plumes, as well in pollution aerosol layers are rare. Therefore we summarize the main findings of these aerosol types in one single table (Table 6). Our results for the analyzed aerosol types agree very well with former findings.

4.1.4 Marine aerosols

For the lidar derived optical properties (δ_p and S_p) of sea-salt particles, the relative humidity plays an important role, as shown in former measurements, as δ_p and S_p depend on the phase (crystalline or liquid) of the particles. The main findings are listed in Table 7. Our results of δ_p and S_p in marine influenced air masses show good agreement with measurements of liquid sea-salt particles.

4.1.5 Ice particles and volcanic ash

We extend our aerosol classification to two key atmospheric aerosol types, ice particles and pure volcanic ash. However, as HSRL measurements of ice particles and pure volcanic ash are unavailable so far, we use literature summarized in Table 8 for the classification.

4.2 Aerosol classification

Tables 4–7 show that values of δ_p and S_p for different aerosol types are not dependent on measurement location and measurement time. Therefore δ_p and S_p can be used to classify the examined aerosol types. Altogether our aerosol classification scheme includes eight main atmospheric aerosol types and mixtures. The type is identified using the particle linear depolarization ratio, the lidar ratio and the color ratio of backscatter (Fig. 8). The threshold values for δ_p, S_p, and CR are defined according to our findings presented in Sect. 3.2, and to values listed in Tables 4–8.

ACPD
12, 25983–26028, 2012

4.3 Aerosol mask

Applying the classification scheme of Fig. 8 to the case studies shown in Sect. 3.1, results in Fig. 9. Figure 9 demonstrates that the aerosol mask is capable to identify the complex stratification during SAMUM-2.

In order to validate the aerosol mask, we use the absorption Angstöm exponent which has been shown to be a good in-situ measure for aerosol types and source regions (e.g. Petzold et al., 2009; Weinzierl et al., 2011). The absorption Angström exponent is only dependent on the aerosol type, and not on its concentration. As an example for the validation of the aerosol mask with coordinated in-situ samples, Fig. 10 shows the absorption Angström exponent (left panel) and the aerosol mask, derived from the aerosol classification scheme presented in Sect. 4.2 (right panel), applied to HSRL results of a measurement flight on 25 January 2008 during the SAMUM-2 field campaign.

Figure 10 shows the good agreement of the aerosol classification from lidar derived optical properties with measurements of the absorption Angström exponent. For the latter, values of about 4.0, typical values for dust and dust mixtures, were found in the lower layer, which was classified as mixed Saharan dust layer from lidar measurements (orange color). In the upper layer values of the Angström exponent of absorption of about 1.5, typically for African biomass burning aerosols (Weinzierl et al., 2011), were found. This is in good agreement with the lidar classification of African biomass burning aerosols in this layer (light green color). Trajectory analysis (Sect. 2.5, Fig. 3) supports these findings.

5 Conclusions

Aerosol classification is needed for many applications in remote sensing of the atmosphere, as well as for better assessment of the Earth's radiation budget. The aerosol type is characterized by a variety of so called intensive optical and microphysical

ACPD
12, 25983–26028, 2012

properties that may partly exhibit large differences. The classification is therefore a delicate process, as it can lead to large errors in the retrieved quantities. The presented work shows the potential of airborne high spectral resolution lidar and depolarization measurements to distinguish between different aerosol types and mixtures by combining two lidar derived intensive aerosol properties, the aerosol lidar ratio, the particle linear depolarization ratio, and the color ratio.

While airborne lidar measurements can be regarded as case studies, satellite measurements provide a global cover of the Earth. The presented approach can also be applied to satellite instruments. Using the measurements of a future polarization-sensitive HSRL system in space (e.g. ATLID onboard EarthCARE), not only the climate relevant optical properties, the aerosol optical thickness and the aerosol extinction coefficient, can be derived without further assumptions of the aerosol type. By simultaneous measurements of S_p and δ_p it would also be possible to directly assign an aerosol type or mixture to a detected aerosol layer.

Finally, combining state-of-the-art HSRL techniques with high-level inversion methods results in a global distribution of high resolution spatial and vertical information of the structure of clouds and aerosols. Together with collocated passive instruments this advanced methodology is expected to further develop our understanding of the relationship between aerosols and radiation, which is an indispensable pre-requisite for an improved prediction of future climate.

Acknowledgements. This work has been funded partly by the Deutsche Forschungsgemeinschaft (DFG) within the Forschergruppe SAMUM (FOR 539), the European Space Agency (ICAROHS contract no. 22169/NL/CT; XXX contract no. 19429/06/NL/AR), the Helmholtz Association (VH-NG-606, Helmholtz-Hochschul-Nachwuchsforschergruppe AerCARE), the EC Integrated Project EUCAARI (No 036833-2), and the HALO-SPP (No. 1294/2). The authors gratefully acknowledge the NOAA Air Resources Laboratory (ARL) for the provision of the HYSPLIT transport and dispersion model and/or READY website used in this publication (http://www.arl.noaa.gov/ready.html). Furthermore we thank Christoph Kiemle for the internal review of this work.

ACPD
12, 25983–26028, 2012

References

Alados-Arboledas, L., Müller, D., Guerrero-Rascado, J. L., Navas-Guzmán, F., Pérez-Ramírez, D., and Olmo, F. J.: Optical and microphysical properties of fresh biomass burning aerosol retrieved by Raman lidar, and star-and sun photometry, Geophys. Res. Lett., 38, L01807, doi:10.1029/2010GL045999, 2011.

Ansmann, A., Riebesell, M., and Weitkamp, C.: Measurement of atmospheric aerosol extinction profiles with a Raman lidar, Opt. Lett., 15, 746–748, doi:10.1364/OL.15.000746, 1990.

Ansmann, A., Wandinger, U., Riebesell, M., Weitkamp, C., and Michaelis, W.: Independent measurement of extinction and backscatter profiles in cirrus clouds by using a combined Raman elastic-backscatter lidar, Appl. Optics, 31, 7113–7113, doi:10.1364/AO.31.007113, 1992.

Ansmann, A., Wandinger, U., Wiedensohler, A., and Leiterer, U.: Lindenberg aerosol characterization experiment 1998 (LACE 98): overview, J. Geophys. Res., 107, 8129, doi:10.1029/2000JD000233, 1998.

Ansmann, A., Bösenberg, J., Chaikovsky, A., Comeron, A., Eckhardt, S., Eixmann, R., Freudenthaler, V., Ginoux, P., Komguem, L., Linne, H., Lopez, M. A., Matthias, V., Mattis, I., Mitev, V., Müller, D., Music, S., Nickovic, S., Pelon, J., Sauvage, L., Sobolewsky, P., Srivastava, M. K., Stohl, A., Torres, O., Vaughn, G., Wandinger, U., and Wiegner, M.: Long-range transport of Saharan dust to Northern Europe: the 11–16 October 2001 outbreak observed with EARLINET, J. Geophys. Res., 108, 4783, doi:10.1029/2003JD003757, 2003.

Ansmann, A., Ingmann, P., Rille, O. L., Lajas, D., and Wandinger, U.: Particle backscatter and extinction profiling with the spaceborne high-spectral-resolution doppler lidar ALADIN: methodology and simulations, Appl. Optics, 45, 6606–6622, doi:10.1364/AO.46.006606, 2007.

Ansmann, A., Baars, H., Tesche, M., Müller, D., Althausen, D., Engelmann, R., Pauliquevis, T., and Artaxo, P.: Dust and smoke transport from Africa to South America: lidar profiling over Cape Verde and the amazon rainforest, Geophys. Res. Lett., 36, L11802, doi:10.1029/2009GL037923, 2009.

Ansmann, A., Tesche, M., Groß, S., Freudenthaler, V., Seifert, P., Hiebsch, A., Schmidt, J., Wandinger, U., Mattis, I., Müller, D., and Wiegner, M.: The 16 April 2010 major volcanic ash plume over Central Europe: EARLINET lidar and AERONET photome-

ACPD
12, 25983–26028, 2012

ter observations at Leipzig and Munich, Germany, Geophys. Res. Lett., 37, L13810, doi:10.1029/2010GL043809, 2010.
Ansmann, A., Petzold, A., Kandler, K., Tegen, I., Wendisch, M., Müller, D., Weinzierl, B., Müller, T., and Heintzenberg, J.: Saharan Mineral dust experiments SAMUM-1 and SAMUM-2: what have we learned?, Tellus B, 63, 403–429, doi:10.1111/j.1600-0889.2011.00555.x, 2011.
Burton, S. P., Ferrare, R. A., Hostetler, C. A., Hair, J. W., Rogers, R. R., Obland, M. D., Butler, C. F., Cook, A. L., Harper, D. B., and Froyd, K. D.: Aerosol classification using airborne High Spectral Resolution Lidar measurements – methodology and examples, Atmos. Meas. Tech., 5, 73–98, doi:10.5194/amt-5-73-2012, 2012.
Chen, W.-N., Tsai, F.-J., Chou, C. C.-K., Chang, S.-Y., Chen, Y.-W., and Chen, J.-P.: Optical properties of Asian dusts in the free atmosphere measured by Raman lidar at Taipei, Taiwan, Atmos. Environ., 41, 7698–7714, doi:10.1016/j.atmosenv.2007.06.001, 2007.
Dinter, T., von Hoyningen-Huene, W., Burrows, J., Kokhanovsky, A., Bierwirth, E., Wendisch, M., Müller, D., Kahn, R., and Diouri, M.: Retrieval of aerosol optical thickness for desert conditions using meris observations during the SAMUM campaign, Tellus B, 61, 229–238, doi:10.1111/j.1600-0889.2008.00391.x, 2009.
Draxler, R. R. and Rolph, G. D.: Hysplit (hybrid single particle lagrangian integrated trajectory) model, NOAA Air Resources Laboratory, Silver Spring, MD, 2012.
ESA: Earth clouds, aerosol, and radiation explorer, Eur. Space Agency Spec. Publ. ESA, SP-1279(1), 2004.
Esselborn, M., Wirth, M., Fix, A., Tesche, M., and Ehret, G.: Airborne high spectral resolution lidar for measuring aerosol extinction and backscatter coefficients, Appl. Optics, 47, 346–358, doi:10.1364/AO.47.000346, 2008.
Esselborn, M., Wirth, M., Fix, A., Weinzierl, B., Rasp, K., Tesche, M., and Petzold, A.: Spatial distribution and optical properties of Saharan dust observed by airborne high spectral resolution lidar during SAMUM 2006, Tellus B, 61, 131–143, doi:10.1111/j.1600-0889.2008.00394.x, 2009.
Freudenthaler, V., Homburg, F., and Jäger, H.: Optical parameters of contrails from lidar measurements: linear depolarization, Geophys. Res. Lett., 23, 3715–3718, doi:10.1029/96GL03646, 1996.
Freudenthaler, V., Esselborn, M., Wiegner, M., Heese, B., Tesche, M., Ansmann, A., Müller, D., Althausen, D., Wirth, M., Fix, A., Ehret, G., Knippertz, P., Toledano, C., Gasteiger, J., Garhammer, M., and Seefeldner, M.: Depolarization ratio profiling at several wavelengths

ACPD
12, 25983–26028, 2012

in pure Saharan dust during SAMUM 2006, Tellus B, 61, 165–179, doi:10.1111/j.1600-0889.2008.00396.x, 2009.

Groß, S., Tesche, M., Freudenthaler, V., Toledano, C., Wiegner, M., Ansmann, A., Althausen, D., and Seefeldner, M.: Characterization of saharan dust, marine aerosols and mixtures of biomass burning aerosols and dust by means of multi-wavelength depolarization- and Raman-measurements during SAMUM-2, Tellus B, 63, 706–724, doi:10.1111/j.1600-0889.2011.00556.x, 2011a.

Groß, S., Gasteiger, J., Freudenthaler, V., Wiegner, M., Geiß, A., Schladitz, A., Toledano, C., Kandler, K., Tesche, M., Ansmann, A., and Wiedensohler, A.: Characterization of the planetary boundary layer during SAMUM-2 by means of lidar measurements, Tellus B, 63, 695–705, doi:10.1111/j.1600-0889.2011.00557.x, 2011b.

Groß, S., Freudenthaler, V., Wiegner, M., Gasteiger, J., Geiß, A., and Schnell, F.: Dual-wavelength linear depolarization ratio of volcanic aerosols: lidar measurements of the Eyjafjallajökull plume over Maisach, Germany, Atmos. Environ., 48, 85–96, doi:10.1016/j.atmosenv.2011.06.017, 2012.

Hamburger, T., McMeeking, G., Minikin, A., Birmili, W., Dall'Osto, M., O'Dowd, C., Flentje, H., Henzing, B., Junninen, H., Kristensson, A., de Leeuw, G., Stohl, A., Burkhart, J. F., Coe, H., Krejci, R., and Petzold, A.: Overview of the synoptic and pollution situation over Europe during the EUCAARI-LONGREX field campaign, Atmos. Chem. Phys., 11, 1065–1082, doi:10.5194/acp-11-1065-2011, 2011.

Hamburger, T., McMeeking, G., Minikin, A., Petzold, A., Coe, H., and Krejci, R.: Airborne in-situ measurements of aerosol microphysical properties in the troposphere above Europe, Atmos. Chem. Phys., submitted, 2012.

Hair, J. W., Hostetler, C. A., Cook, A. L., Harper, D. B., Ferrare, R. A., Mack, T. L., Welch, W., Izquierdo, L. R., and Hovis, F. E.: Airborne high spectral resolution lidar for profiling aerosol optical properties, Appl. Optics, 47, 6734–6752, 2008.

Heintzenberg, J.: The SAMUM-1 experiment over Southern Morocco: overview and introduction, Tellus B, 61, 2–11, doi:10.1111/j.1600-0889.2008.00403.x, 2009.

Ingmann, P.: EarthCARE – earth clouds, aerosols, and radiation explorer, Tech. Rep., ESA, Sp-1279(1), 2004.

IPCC: Climate Change 2007: The scientific basis, edited by: Solomon, S., Qin, D., Manning, M., Chen, Z., Marquis, M., Averyt, K. B., Tignor, M., and Miller, H. L., Cambridge University Press, 2007.

ACPD
12, 25983–26028, 2012

Kahn, R., Petzold, A., Wendisch, M., Bierwirth, E., Dinter, T., Esselborn, M., Fiebig, M., Heese, B., Knippertz, P., Müller, D., Schladitz, A., and von Hoyningen-Huene, W.: Desert dust aerosol air mass mapping in the Western Sahara, using particle properties derived from space-based multi-angle imaging, Tellus B, 61, 239–251, doi:10.1111/j.1600-0889.2008.00398.x, 2009.

Kandler, K., Schütz, L., Jäckel, S., Lieke, K., Emmel, C., Müller-Ebert, D., Schladitz, A., Segvic, B., Wiedensohler, A., and Weinbruch, S.: Ground-based off-line aerosol measurements at praia, cape verde, during the Saharan mineral dust experiment campaign: microphysical properties and mineralogical, Tellus B, 63, 459–474, doi:10.1111/j.1600-0889.2011.00546.x, 2011.

Kulmala, M., Asmi, A., Lappalainen, H. K., Carslaw, K. S., Pöschl, U., Baltensperger, U., Hov, Ø., Brenquier, J.-L., Pandis, S. N., Facchini, M. C., Hansson, H.-C., Wiedensohler, A., and O'Dowd, C. D.: Introduction: European Integrated Project on Aerosol Cloud Climate and Air Quality interactions (EUCAARI) – integrating aerosol research from nano to global scales, Atmos. Chem. Phys., 9, 2825–2841, doi:10.5194/acp-9-2825-2009, 2009.

Lieke, K., Kandler, K., Emmel, C., Petzold, A., Weinzierl, B., Scheuvens, D., Ebert, M., Weinbruch, S., and Schütz, L.: Particle chemical properties in the vertical column based on aircraft observations in the vicinity of Cape Verde, Tellus B, 63, 497–511, doi:10.1111/j.1600-0889.2011.00553.x, 2011.

Liu, Z., Sugimoto, N., and Murayama, T.: Extinction-to-backscatter ratio of Asian dust observed with high-spectral resolution lidar and Raman lidar, Appl. Optics, 41, 2760–2767, 2002.

Liu, Z., Omar, A., Vaughan, M., Hair, J., Kittaka, C., Hu, Y., Powell, K., Trepte, C., Winker, D., Hostetler, C., Rerrare, R., and Pierce, R.: Calipso lidar observations of the optical properties of Saharan dust: a case study of long-range transport, J. Geophys. Res., 113, D07207, doi:10.1029/2007JD008878, 2008.

Mattis, I., Ansmann, A., Müller, D., Wandinger, U., and Althausen, D.: Dual-wavelength raman lidar observations of the extinction-to-backscatter ratio of Saharan dust, Geophys. Res. Lett., 29, 1306, doi:10.1029/2002GL014721, 2002.

Mishchenko, M. I. and Sassen, K.: Depolarization of lidar returns by small ice crystals: An application to contrails, Geophys. Res. Lett., 25, 309–312, doi:10.1029/97GL03764, 1998.

Mona, L., Amodeo, A., Pandolfi, M., and Pappalardo, G.: Saharan dust intrusions in the Mediterranean area: three years of Raman lidar measurements, J. Geophys. Res., 111, D16203, doi:10.1029/2005JD006569, 2006.

ACPD
12, 25983–26028, 2012

Müller, D., Mattis, I., Wandinger, U., Ansmann, A., and Althausen, D.: Raman lidar observations of aged Siberian and Canadian forest fire smoke in the free troposphere over Germany in 2003: microphysical particle characterization, J. Geophys. Res., 110, D17201, doi:10.1029/2004JD005756, 2005.

Müller, D., Ansmann, A., Mattis, I., Tesche, M., Wandinger, U., Althausen, D., and Pisani, G.: Aerosol-type-dependent lidar ratios observed with Raman lidar, J. Geophys. Res., 112, D16202, doi:10.1029/2006JD008292, 2007.

Müller, D., Kolgotin, A., Mattis, I., Petzold, A. and Stohl, A.: Vertical profiles of microphysical particle properties derived from inversion with two-dimensional regularization of multiwavelength Raman lidar data: experiment, Appl. Optics, 50, 2069–2079, 2011.

Müller, T., Schladitz, A., Kandler, K., and Wiedensohler, A.: Spectral particle absorption coefficients, single scattering albedos, and imaginary parts of refractive indices from ground based in-situ measurements at Cape Verde island during SAMUM-2, Tellus B, 63, 573–588, doi:10.1111/j.1600-0889.2011.00572.x, 2011.

Murayama, T., Okamoto, H., Kaneyasu, N., Kamataki, H., and Miura, K.: Application of lidar depolarization measurement in the atmospheric boundary layer: effects of dust and sea-salt particles, J. Geophys. Res., 104, 31781–31792, doi:10.1029/1999JD900503, 1999.

Murayama, T., Masonis, S. J., Redemann, J., Anderson, T. L., Schmid, B., Livingston, J. M., Russell, P. B., Huebert, B., Howell, S. G., McNaughton, C. S., Clarke, A., Abo, M., Shimizu, A., Sugimoto, N. Yabuki, M., Kuze, H., Fukagawa, S., Maxwell-Meier, K., Weber, R. J., Orsini, D. A., Blomquist, B., Bandy, A., and Thornton, D.: An intercomparison of lidar-derived aerosol optical properties with airborne measurements near Tokyo during ACE-Asia, J. Geophys. Res., 108, 8651, doi:10.1029/2002JD003259, 2003.

Murayama, T., Müller, D., Wada, K., Shimizu, A., Sekiguchi, M., and Tsukamoto, T.: Characterization of Asian dust and Siberian smoke with multiwavelength raman lidar over Tokyo, Japan in spring 2003, Geophys. Res. Lett., 31, L23103, doi:10.1029/2004GL021105, 2004.

Noh, Y. M., Kima, Y. J., and Müller, D.: Seasonal characteristics of lidar ratios measured with a Raman lidar at Gwangju, Korea in spring and autumn, Atmos. Environ., 42, 2208–2224, doi:10.1016/j.atmosenv.2007.11.045, 2008.

Omar, A., Winker, D. M., Vaughan, M. A., Hu, Y., Trepte, C. R., Ferrare, R. A., Lee, K.-P., Hostetler, C. A., Kittaka, C., Rogers, R. R., Kuehn, R. E., and Liu, Z.: The calipso automated aerosol classification and lidar ratio selection algorithm, J. Atmos. Ocean. Tech., 26, 1994–2014, doi:10.1175/2009jtecha1231.1, 2009.

ACPD
12, 25983–26028, 2012

Papayannis, A., Mamouri, R. E., Amiridis, V., Remoundaki, E., Tsaknakis, G., Kokkalis, P., Veselovskii, I., Kolgotin, A., Nenes, A., and Fountoukis, C.: Optical-microphysical properties of Saharan dust aerosols and composition relationship using a multi-wavelength Raman lidar, in situ sensors and modelling: a case study analysis, Atmos. Chem. Phys., 12, 4011–4032, doi:10.5194/acp-12-4011-2012, 2012.

Petzold, A., Fiebig, M., Flentje, H., Keil, A., Leiterer, U., Schröder, F., Stifter, A., Wendisch, M., and Wendling, P.: Vertical variability of aerosol properties observed at a continental site during the Lindenberg Aerosol Characterization Experiment (LACE 98), J. Geophys. Res., 107, 8128, doi:10.1029/2001JD001043, 2002.

Petzold, A., Weinzierl, B., Huntrieser, H., Stohl, A., Real, E., Cozic, J., Fiebig, M., Hendricks, J., Lauer, A., Law, K., Roiger, A., Schlager, H., and Weingartner, E.: Perturbation of the European free troposphere aerosol by North American forest fire plumes during the ICARTT-ITOP experiment in summer 2004, Atmos. Chem. Phys., 7, 5105–5127, doi:10.5194/acp-7-5105-2007, 2007.

Petzold, A., Hasselbach, J., Lauer, P., Baumann, R., Franke, K., Gurk, C., Schlager, H., and Weingartner, E.: Experimental studies on particle emissions from cruising ship, their characteristic properties, transformation and atmospheric lifetime in the marine boundary layer, Atmos. Chem. Phys., 8, 2387–2403, doi:10.5194/acp-8-2387-2008, 2008.

Petzold, A., Rasp, K., Weinzierl, B., Esselborn, M., Hamburger, T., Dörnbrack, A., Kandler, K., Schütz, L., Knippertz, P., Fiebig, M., and Virkkula, A.: Saharan dust absorption and refractive index from aircraft-based observations during SAMUM 2006, Tellus B, 61, 118–130, doi:10.1111/j.1600-0889.2008.00383.x, 2009.

Petzold, A., Esselborn, M., Weinzierl, B., Ehret, G., Ansmann, A., Müller, D., Donovan, D., van Zadelhoff, G.-J., Berthier, S., Wiegner, M., Gasteiger, J., Buras, R., Mayer, B., Lajas, D., and Wehr, T.: ICAROHS – Inter-Comparison of Aerosol Retrievals and Observational Requirements for Multi-Wavelength HSRL Systems, Final Report, 22169/NL/CT–STSE-ICAROHS TN1, ESA, 102 pp., 2011.

Preißler, J., Wagner, F., Pereira, S. N., and Guerrero-Rascado, J. L.: Multi-instrumental observation of an exceptionally strong Saharan dust outbreak over Portugal, J. Geophys. Res., 116, D24204, doi:10.1029/2011JD016527, 2011.

Quinn, P. K., Anderson, T. L., Bates, T. S., Dlugi, R., Heintzenberg, J., von Hoyningen-Huene, W., Kulmala, M., Russel, P. B., and Swietlicki, E.: Closure in tropospheric aerosol-

ACPD
12, 25983–26028, 2012

climate research: a review and future needs for addressing aerosol direct short-wave radiative forcing, Atmos. Phys., 69, 547–577, 1996.
Reitebuch, O., Lemmerz, C., Nagel, E., Paffrath, U., Durand, Y., Endemann, M., Fabre, F., and Chaloupy, M.: The airborne demonstrator for the direct-detection doppler wind lidar aladin on ADM-Aeolus, Part i: Instrument design and comparison to satellite instrument, J. Atmos. Ocean. Tech., 26, 2501–2515, 2009.
Sakai, T., Shibata, T., Kwon, S.-A., Kim, Y.-S., Tamura, K., and Iwasaka, Y.: Free tropospheric aerosol backscatter, depolarization ratio, and relative humidity measured with the Raman lidar at Nagoya in 1994–1997: contributions of aerosols from the asian continent and the pacific ocean, Atmos. Environ., 34, 431–442, doi:10.1016/S1352-2310(99)00328-3, 2000.
Sakai, T., Tetsu, S., Iwasaka, Y., Nagai, T., Nakazato, M., Matsumura, T., Ichiki, A., Kim, Y.-S., Tamura, K., Troshkin, D., and Hamdi, S.: Case study of Raman lidar measurements of Asian dust events in 2000 and 2001 at Nagoya and Tsukuba, Japan, Atmos. Environ., 36, 5479–5489, doi:10.1016/S1352-2310(02)00664-7, 2002.
Sakai, T., Nagai, T., Nakazato, M., Mano, Y., and Matsumura, T.: Ice clouds and Asian dust studied with lidar measurements of particle extinction-to-backscatter ratio, particle depolarization, and water-vapor mixing ratio over Tsukuba, Appl. Optics, 42, 7103–7116, 2003.
Sakai, T., Nagai, T., Zaizen, Y., and Mano, Y.: Backscattering linear depolarization ratio measurements of mineral, sea salt, and ammonium sulfate particles simulated in a laboratory chamber, Appl. Optics, 49, 4441–4449, doi:10.1364/AO.49.004441, 2010.
Sassen, K. and Hsueh, C.: Contrail properties derived from high-resolution polarization lidar studies during SUCCESS, Geophys. Res. Lett., 25, 1165–1168, doi:10.1029/97GL03503, 1998.
Shimizu, H., Lee, S., and She, C.: High spectral resolution lidar system with atomic blocking filters for measuring atmospheric parameters, Appl. Optics, 22, 1373–1381, 1983.
Shipley, S., Tracy, D., Eloranta, E., Trauger, J., Sroga, J., Roesler, F., and Weinman, J.: High spectral resolution lidar to measure optical scattering properties of atmospheric aerosols, 1: Theory and instrumentation, Appl. Optics, 22, 3716–3724, 1983.
Stohl, A., Eckhardt, S., Forster, C., James, P., Spichtinger, N., and Seibert, P.: A replacement for simple back trajectory calculations in the interpretation of atmospheric trace substance measurements, Atmos. Environ., 36, 4635–4648, 2002.
Tesche, M., Ansmann, A., Müller, D., Althausen, D., Mattis, I., Heese, B., Freudenthaler, V., Wiegner, M., Esselborn, M., Pisani, G., and Knippertz, P.: Vertical profiling of saharan dust

ACPD
12, 25983–26028, 2012

with Raman lidars and airborne HSRL in Southern Morocco during SAMUM, Tellus B, 61, 144–164, doi:10.1111/j.1600-0889.2008.00390.x, 2009a.

Tesche, M., Ansmann, A., Müller, D., Althausen, D., Engelmann, R., Freudenthaler, V., and Groß, S.: Vertically resolved separation of dust and smoke over Cape Verde using multiwavelength Raman and polarization lidars during Saharan mineral dust experiment 2008, J. Geophys. Res., 114, D13202, doi:10.1029/2009JD011862, 2009b.

Tesche, M., Gross, S., Ansmann, A., Müller, D., Althausen, D., Freudenthaler, V., and Esselborn, M.: Profiling of Saharan dust and biomass-burning smoke with multiwavelength polarization Raman lidar at Cape vVerde, Tellus B, 63, 649–676, doi:10.1111/j.1600-0889.2011.00548.x, 2011.

Tsunematsu, N., Nagai, T., Murayama, T., Adachi, A., Murayama, Y.: Volcanic ash transport from Mount Asama to The Tokyo Metropolitan area influenced by large-scale local wind circulation, J. Appl. Meteorol. Clim., 47, 1248–1265, doi:10.1175/2007JAMC1644.1, 2008.

Wandinger, U., Müller, D., Böckmann, C., Althausen, D., Matthias, V., Bösenberg, J., Weiß, V., Fiebig, M., Wendisch, M., Stohl, A., and Ansmann, A.: Optical and microphysical characterization of biomass-burning and industrial-pollution aerosols from multiwavelength lidar and aircraft measurements, J. Geophys. Res., 117, 8125, doi:10.1029/2000JD000202, 2002.

Wandinger, U., Tesche, M., Seifert, P., Ansmann, A., Müller, D., and Althausen, D.: Size matters: influence of multiple scattering on CALIPSO light-extinction profiling in desert dust, Geophys. Res. Lett., 37, L10801, doi:10.1029/2010GL042815, 2010.

Weinzierl, Petzold, B. A., Esselborn, M., Wirth, M., Rasp, K., K. Kandler, Schütz, L., Köpke, P., and Fiebig, M.: Airborne measurements of dust layer properties, particle size distribution and mixing state of Saharan dust during SAMUM 2006, Tellus B, 61, 96–117, doi:10.1111/j.1600-0889.2008.00392.x, 2009.

Weinzierl, B., Sauer, D., Esselborn, M., Petzold, A., Veira, A., Rose, M., Mund, S., Wirth, M., Ansmann, A., Tesche, M., Gross, S., and Freudenthaler, V.: Microphysical and optical properties of dust and tropical biomass burning aerosol layers in the Cape Verde region – an overview of the airborne in situ and lidar measurements during SAMUM-2, Tellus B, 63, 589–618, doi:10.1111/j.1600-0889.2011.00566.x, 2011.

Wiegner, M., Gasteiger, J., Groß, S., Schnell, F., Freudenthaler, V., and Forkel, R.: Characterization of the Eyjafjallajökull ash-plume: potential of lidar remote sensing, Phys. Chem. Earth Pt. A/B/C, 45–46, 79–86, doi:10.1016/j.pce.2011.01.006, 2012.

ACPD
12, 25983–26028, 2012

Winker, D. M., Hunt, W. H., and McGill, M. J.: Initial performance assessment of caliop, Geophys. Res. Lett., 34, L19803, doi:10.1029/2007GL030135, 2007.
Wirth, M., Fix, A., Mahnke, P., Schwarzer, H., Schrandt, F., and Ehret, G.: The airborne multi-wavelength water vapor differential absorption lidar WALES: system design and performance, Appl. Phys. B-Lasers O., 96, 201–213, doi:10.1007/s00340-009-3365-7, 2009.
Xie, C., Nishizawa, T., Sugimoto, N., Matsui, I., and Wang, Z.: Characteristics of aerosol optical properties in pollution and Asian dust episodes over Beijing, China, Appl. Optics, 47, 4945–4951, 2008.

ACPD
12, 25983–26028, 2012

Table 1. Detailed information about analyzed case studies used for the aerosol classification concerning aerosol type, measurement experiment, date, location, time and altitude range of observation.

Aerosol type	Experiment	Date	Lat	Lon	Time (UTC)	Altitude (km)
Mineral dust	SAMUM-1	19 May 2006	30.9	−7.6	11:09	2.0–5.0
		28 May 2006	30.1	−6.5	10:40	1.0–4.0
		3 Jun 2006	30.9	−6.9	07:40	1.0–4.0
		4 Jun 2006	30.9	−6.9	09:47	1.5–4.5
Mixed dust	SAMUM-2	19 Jan 2008	19.0	21.5	16:45	0.5–1.0
		25 Jan 2008	14.9	−22.3	15:10	0.8–1.2
		28 Jan 2008	17.5	−22.2	10:30	1.0–1.4
		29 Jan 2008	14.9	−21.5	13:20	0.8–1.2
		4 Feb 2008	12.6	−21.1	16:00	0.8–1.2
BBA*	SAMUM-2	19 Jan 2008	19.0	21.5	16:45	2.5–3.5
		23 Jan 2008	11.2	−19.9	17:15	2.0–3.0
		4 Feb 2008	12.6	−21.1	16:00	3.0–4.0
		5 Feb 2008	14.9	−22.5	15:00	3.5–4.0
		5 Feb 2008	14.8	−21.9	17:45	3.5–4.0
Marine	SAMUM-2	19 Jan 2008	36.5	−9.8	11:30	0.2–0.4
		4 Feb 2008	12.6	−21.1	16:00	0.1–0.3
		5 Feb 2008	14.9	−22.5	15:00	0.1–0.3
		5 Feb 2008	14.8	−21.9	17:45	0.1–0.3
		9 Feb 2008	21.9	−19.7	10:00	0.5–1.0
Pollution	EUCAARI	6 May 2008	52.8	1.6	11:02	0.5–1.3
		6 May 2008	51.4	11.4	16:08	1.3–2.3
		8 May 2008	51.4	5.7	14:45	0.1–1.3
		14 May 2008	51.4	−12.9	11:30	0.5–1.5
BBC**	LACE98	9 Aug 1998	52.0	14.2	22:40	4.5–5.3

* Biomass burning Africa
** Biomass burning Canada

ACPD
12, 25983–26028, 2012

Table 2. Mean value ± standard deviation of aerosol lidar ratio, particle linear depolarization ratio and color ratio of backscatter for the examined aerosol types, as well as value of maximum density per bin, range, and median. The data in brackets give the counts per bin.

Aerosol Type	Mean ± stdv	Value of maximum frequency	Range	Median
Aerosol lidar ratio (sr) at 532 nm				
Saharan dust	48 ± 5	47 (1538)	33–68	48
Mixed Saharan dust	50 ± 4	48 (1348)	32–71	49
Biomass burning aerosol (Africa)	63 ± 7	60 (1601)	36–91	62
Biomass burning aerosol (Canada)	69 ± 17	61 (485)	0–276	65
Marine aerosol (North Atlantic)	18 ± 5	18 (687)	0–33	18
Anthropogenic pollution aerosol (Europe)	56 ± 6	61 (485)	33–72	56
Particle linear depolarization ratio (%) at 532 nm				
Saharan dust	32 ± 2	32 (806)	25–43	32
Mixed Saharan dust	27 ± 2	28 (1034)	21–31	27
Biomass burning aerosol (Africa)	14 ± 2	15 (1245)	8–26	14
Biomass burning aerosol (Canada)	7 ± 2	6 (188)	0–32	7
Marine aerosol (North Atlantic)	3 ± 1	2 (2596)	1–11	2
Anthropogenic pollution aerosol (Europe)	6 ± 1	6 (686)	3–11	6
Color ratio of backscatter at 532 nm				
Saharan dust	1.30 ± 0.15	1.29 (913)	0.7–2.56	1.3
Mixed Saharan dust	1.48 ± 0.09	1.46 (1134)	1.16–1.96	1.48
Biomass burning aerosol (Africa)	1.63 ± 0.13	1.62 (1651)	1.04–2.41	1.63
Biomass burning aerosol (Canada)	4.70 ± 1.30	4.43 (108)	1.40–16.2	4.62
Marine aerosol (North Atlantic)	1.64 ± 0.10	1.6 (773)	1.17–2.62	1.64
Anthropogenic pollution aerosol (Europe)	2.43 ± 0.27	2.3 (209)	1.72–3.45	2.41

ACPD
12, 25983–26028, 2012

Table 3. Values of the particle linear depolarization ratio (PDR) and the lidar ratio calculated for selected mixing ratios of marine aerosol and Saharan dust, and of Canadian biomass burning aerosol (CBB) and Saharan dust. The Saharan dust contribution (SD contribution) refers to the fraction of Saharan dust to the total particle extinction coefficient at 532 nm.

SD contribution	PDR (%)	Lidar ratio (sr)	PDR (%)	Lidar ratio (sr)
	Marine – Saharan Dust		CBB – Saharan Dust	
0 %	3 ± 1	18 ± 5	7 ± 2	59 ± 17
20 %	5 ± 2	21 ± 5	13 ± 1	63 ± 13
40 %	8 ± 3	24 ± 6	18 ± 2	59 ± 10
60 %	12 ± 2	29 ± 6	23 ± 2	55 ± 8
80 %	19 ± 2	36 ± 6	28 ± 2	51 ± 6
100 %	32 ± 2	48 ± 5	32 ± 2	48 ± 5

ACPD
12, 25983–26028, 2012

Table 4. Summary of the key findings concerning the lidar ratio and the particle linear depolarization ratio (PDR) found in pure desert dust layers.

Source	Lidar ratio (sr)	PDR (%)	Comments	Location
Sakai et al. (2002)	46 ± 5		Fresh Gobi dust	Nagoya, Japan
Liu et al. (2002)	42–55		Asian Dust	Tokyo, Japan
Tesche et al. (2009a)	56 ± 5		Fresh Saharan dust	SAMUM-1, Morocco
Groß et al. (2011a)	62 ± 5	31 ± 1	Higher iron content than during SAMUM-1	SAMUM-2a, Cape Verde Islands
Tesche et al. (2011)	54 ± 10	31 ± 1	PDR calculated from 710 nm	SAMUM-2b, Cape Verde Islands
Murayama et al. (2003)	54 ± 9	~ 30	Asian Dust	Tokyo, Japan
Liu et al. (2008)		~ 32	CALIPSO measurements	Transport over the Atlantic Ocean
Freudenthaler et al. (2009)		32 ± 2	Fresh Saharan dust	SAMUM-1, Morocco
Our findings	48 ± 5	31 ± 2	Fresh Saharan dust	SAMUM-1, Morocco

ACPD
12, 25983–26028, 2012

Table 5. Summary of the key findings concerning the lidar ratio and the particle linear depolarization ratio (PDR) found for desert dust mixtures.

Source	Lidar ratio (sr)	PDR (%)	Comments	Location
Ansmann et al. (2003)	40–80	15–20	Unknown mixture	Central Europe
Murayama et al. (2004)	43 ± 7	∼ 20	Unknown mixture	Tokyo Asian dust
Chen et al. (2007)		14 ± 6	Unknown mixture	Taiwan, Asian dust
Groß et al. (2011a)		19–28	Mixtures with biomass burning aerosols and marine aerosols	SAMUM-2a, Cape Verde Islands
Preißler et al. (2011)	53 ± 7	28 ± 4	Unknown mixture	Portugal
Mattis et al. (2002)		40–80	Unknown mixture	Central Europe
Mona et al. (2006)	∼ 57		Unknown mixture	Potenza, Italy
Papayannis et al. (2012)	45–75		Unknown mixture	Athens, Greece
Xie et al. (2008)	38 ± 10	20 ± 3	Unknown mixture	Beijing, China
Our findings	50 ± 4	27 ± 2		SAMUM-2a, Cape Verde Islands

ACPD
12, 25983–26028, 2012

Table 6. Summary of the key findings concerning the lidar ratio and the particle linear depolarization ratio (PDR) found in fresh and aged biomass burning aerosol plumes and for anthropogenic pollution.

Source	Lidar ratio (sr)	PDR (%)	Comments	Location
Fresh biomass burning				
Tesche et al. (2011)	67 ± 12	15 ± 5		Samum 2
Groß et al. (2011)	69 ± 8	16 ± 1		Samum 2
Alados-Arboledas et al. (2011)	60–65			Granada, Spain
Our findings	63 ± 7	14 ± 2		SAMUM-2a, Cape Verde Islands
Aged biomass burning				
Wandinger et al. (2002)	40–80		Canadian biomass burning	Central Europe LACE98
Müller et al. (2005)	26–87	2–3	Canadian and Siberian smoke	Central Europe
Murayama et al. (2003)	∼ 65	5–8	Siberian smoke	Tokyo, Japan
Noh et al. (2009)	63 ± 7		Siberian smoke	Korea
Ansmann et al. (2009b)	60–70	4–5	Aged African biomass burning	Manaus, Brazil
Our findings	69 ± 17	7 ± 2		LACE98, Central Europe
Anthropogenic pollution				
Wandinger et al. (2002)	∼ 50			Central Europe
Xie et al. (2008)	61 ± 14	∼ 7	Moderate pollution	Beijing, China
	44 ± 8	∼ 7	Heavy pollution	Beijing, China
Our findings	55 ± 6	6 ± 1		LACE98, Central Europe

ACPD
12, 25983–26028, 2012

Table 7. Summary of the key findings concerning the lidar ratio and the particle linear depolarization ratio (PDR) found for marine aerosols.

Source	Lidar ratio (sr)	PDR (%)	Comments	Location
Murayama et al. (1999)		1–10	Lower values attributed to liquid sea-salt particles, higher values to crystalline sea-salt	Coastal area of Tokyo Bay, Japan
Sakai et al. (2000)		10 < 5	Relative humidity > 50 % High relative humidity	Nagoya, Japan influenced from Pacific Ocean
Sakai et al. (2010)		1 8	Liquid sea-salt Sea-salt crystals	Laboratory chamber
Groß et al. (2011b)	18 ± 2	1–3	Relative humidity > 50 %	SAMUM-2a, Cape Verde Islands
Our findings	18 ± 5	3 ± 1		SAMUM-2a, Cape Verde Islands

ACPD
12, 25983–26028, 2012

Table 8. Summary of the key findings concerning the lidar ratio and the particle linear depolarization ratio (PDR) found for ice particles and pure volcanic ash layers.

Source	Lidar ratio (sr)	PDR (%)	Comments	Location
Ice particles				
Mischenko and Sassen (1998)		30–70	Contrails	T-Matrix calculations
Sassen and Hsueh (1998)		30–45	Cirrus clouds	North America
		60–70	Contails	
Freudenthaler et al. (1996)		∼ 50	Contrails	Central Europe
Sakai et al. (2003)	< 30		Cirrus clouds	Tsukuba, Japan
Ansmann et al. (1992)	2–20		Cirrus clouds	Central Europe
Burton et al. (2012)	∼ 20		Cirrus clouds	North America
Volcanic ash				
Ansmann et al. (2010)	50–65	∼ 35	Eyjafjallajökull	Central Europe
Groß et al. (2012)	50 ± 5	35–38	Eyjafjallajökull	Central Europe
Wiegner et al. (2012)	49 ± 4	∼ 37	Eyjafjallajökull	Central Europe
Tsunematsu et al. (2008)		> 30	Mount Asama	Japan

ACPD
12, 25983–26028, 2012

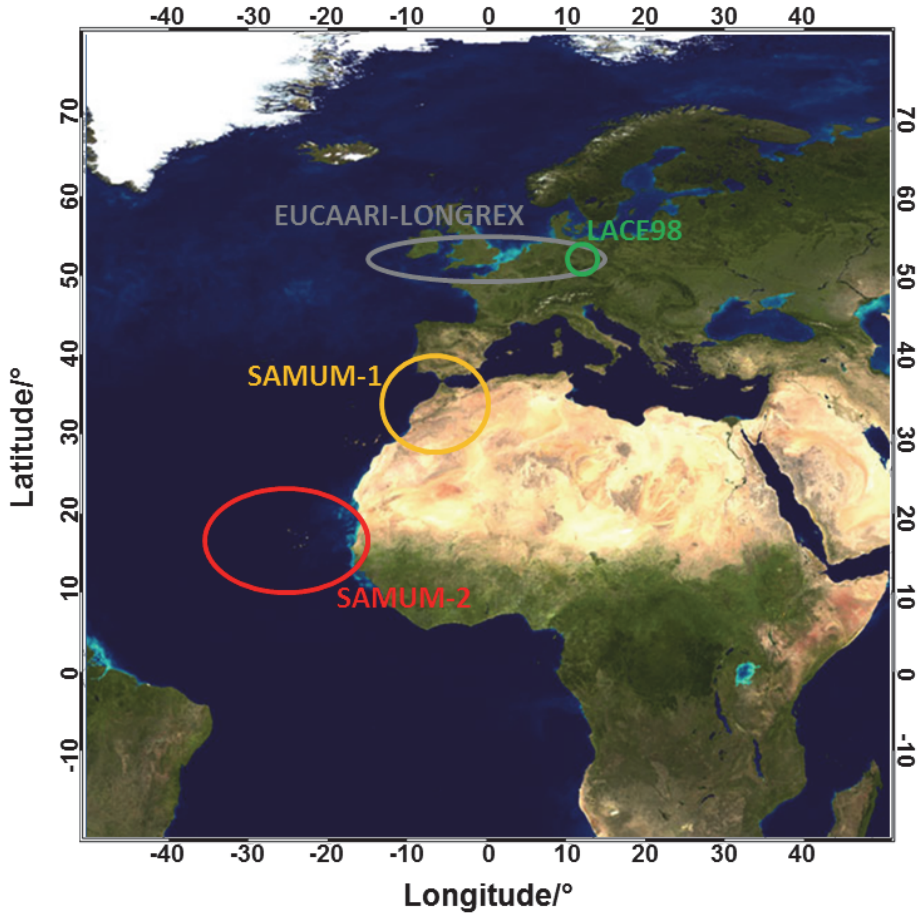

Fig. 1. Main measurement areas of the four considered field experiments on underlying Blue Marble monthly global images for July from NASA's Earth observatory (http://earthobservatory.nasa.gov/Features/BlueMarble).

ACPD
12, 25983–26028, 2012

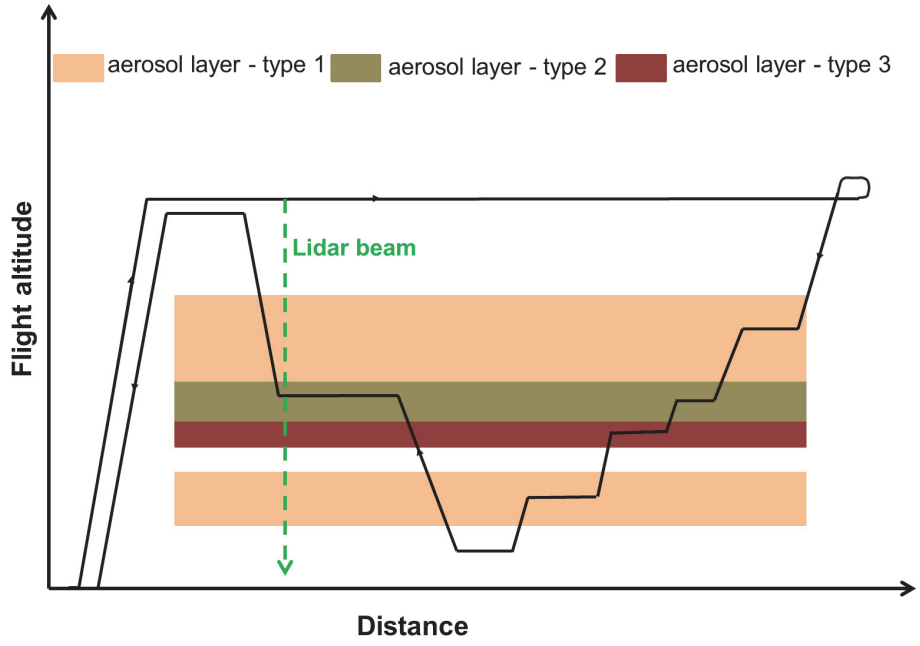

Fig. 2. Flight strategy for coordinated remote sensing and in-situ measurements.

ACPD
12, 25983–26028, 2012

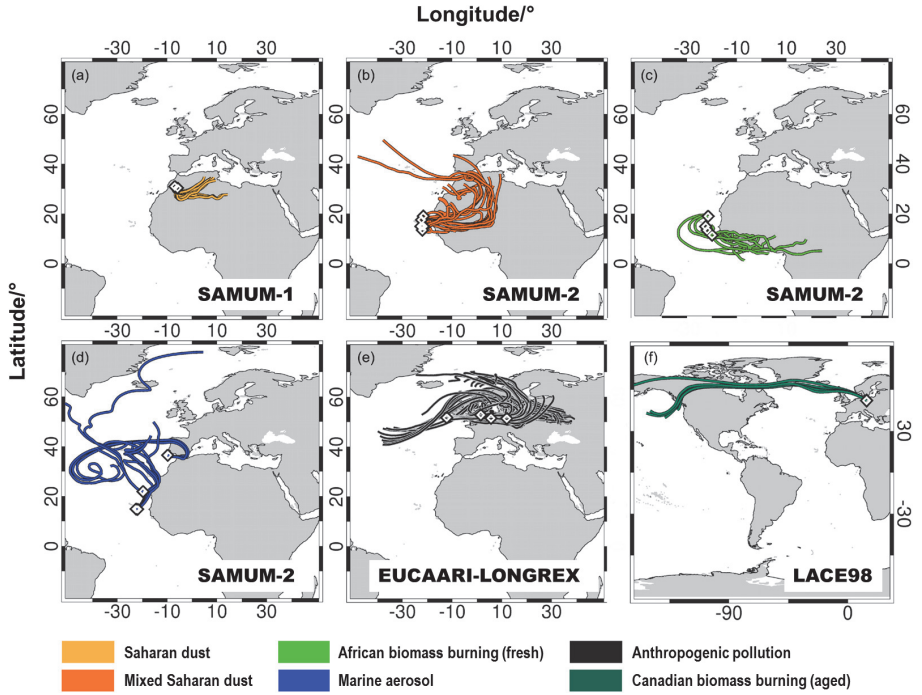

Fig. 3. Backward trajectories for the aerosol layers detected by HSRL measurements and of different origin observed during the LACE98, SAMUM-1, SAMUM-2 and EUCAARI field campaigns. Trajectories date back 5 days for (**a**, **b**, **d** and **e**), and 7 days for (**c** and **f**).

ACPD
12, 25983–26028, 2012

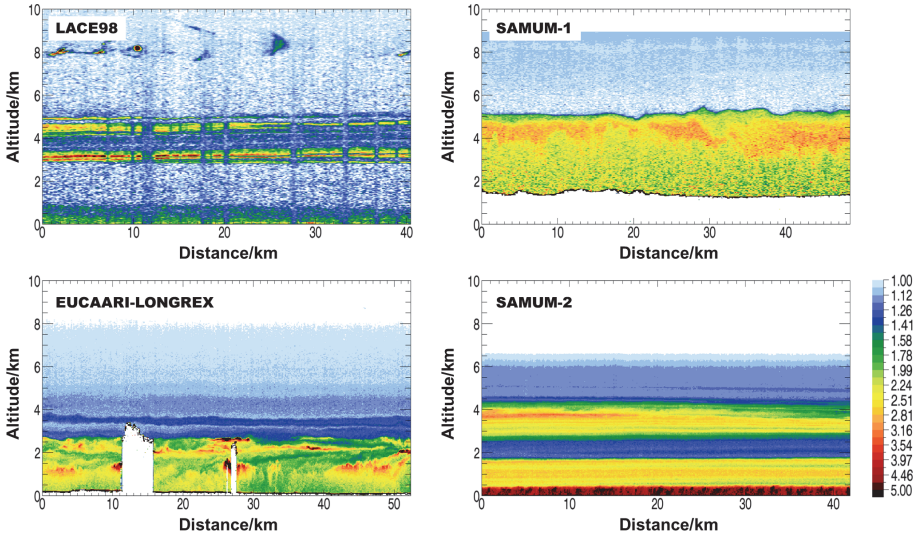

Fig. 4. Selected backscatter ratio cross-sections measured with the HSRL at 532 nm on 9 August 1998 (LACE98), 6 May 2008 (EUCAARI-LONGREX), 19 May 2006 (SAMUM-1), and 4 February 2008 (SAMUM-2). Each cross-section is representative for one field experiment and shows the typical vertical structure of the aerosol load during the respective campaign. All cross-sections have the same color-scale.

ACPD
12, 25983–26028, 2012

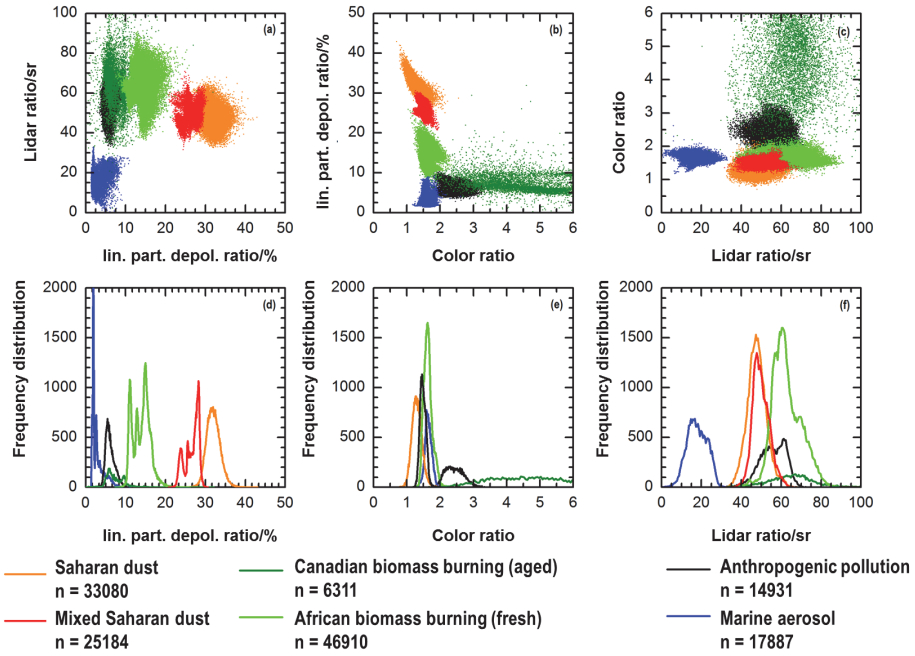

Fig. 5. Characteristic lidar quantities of various atmospheric aerosol types **(a–c)** with frequency distribution **(d–f)**, as well as the total number of measurement points (*n*) for each aerosol type.

ACPD
12, 25983–26028, 2012

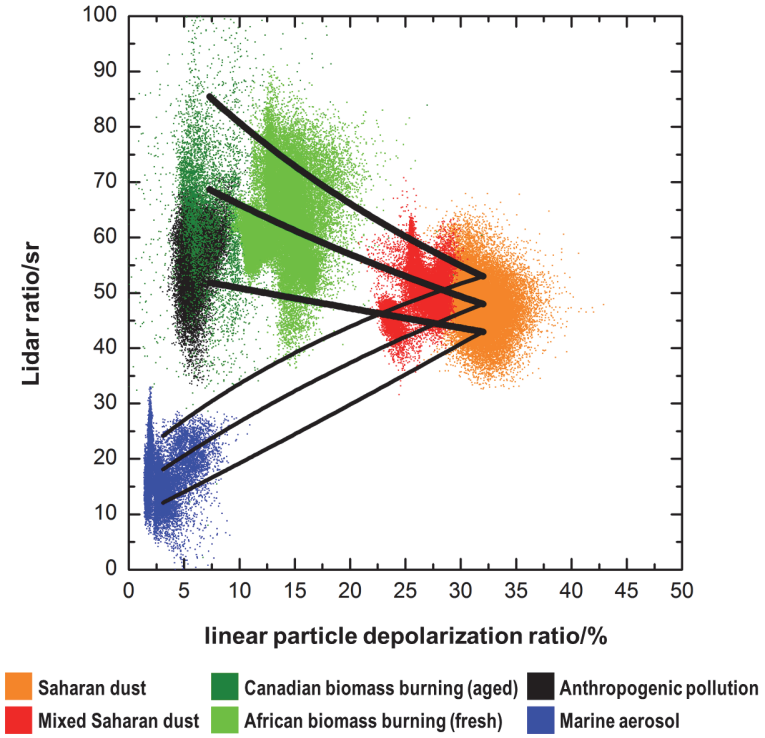

Fig. 6. Aerosol lidar ratio vs. particle linear depolarization ratio for various atmospheric aerosol types and mixing lines for Saharan dust and Canadian Biomass Burning Aerosol (thick lines), and for Saharan dust and Marine aerosol (thin lines). The central line in each case corresponds to the mean values as input for the calculation; the outer lines depict the maximum and minimum range when regarding the uncertainties of the input values.

ACPD
12, 25983–26028, 2012

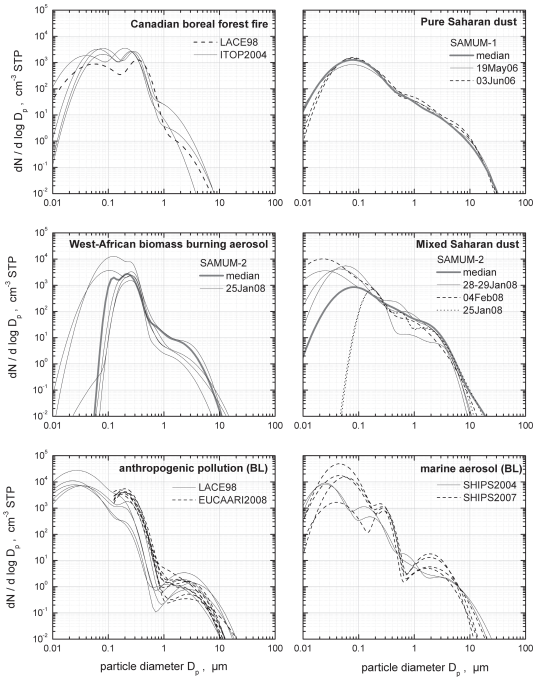

Fig. 7. Representative particle number size distributions for the classified aerosol types: Top left: Canadian boreal forest fire aerosol (LACE98, Petzold et al., 2002, and ICARTT-ITOP 2004, Petzold et al., 2007); mid left: biomass burning aerosol from West African savannah fires (SAMUM-2 (Weinzierl et al., 2011)); bottom left: anthropogenic pollution aerosol over Central Europe (LACE98, Petzold et al., 2002, and EUCAARI 2008, Hamburger et al., 2012); top right: pure Saharan mineral dust over Morocco (SAMUM-1, Weinzierl et al., 2009); mid right: Saharan mineral dust mixed with biomass burning aerosol over Cape Verde Islands (SAMUM-2, Weinzierl et al., 2011); bottom right: marine boundary layer aerosol over the North Atlantic (SHIPS 2004, Petzold et al., 2008, and SHIPS 2007).

ACPD
12, 25983–26028, 2012

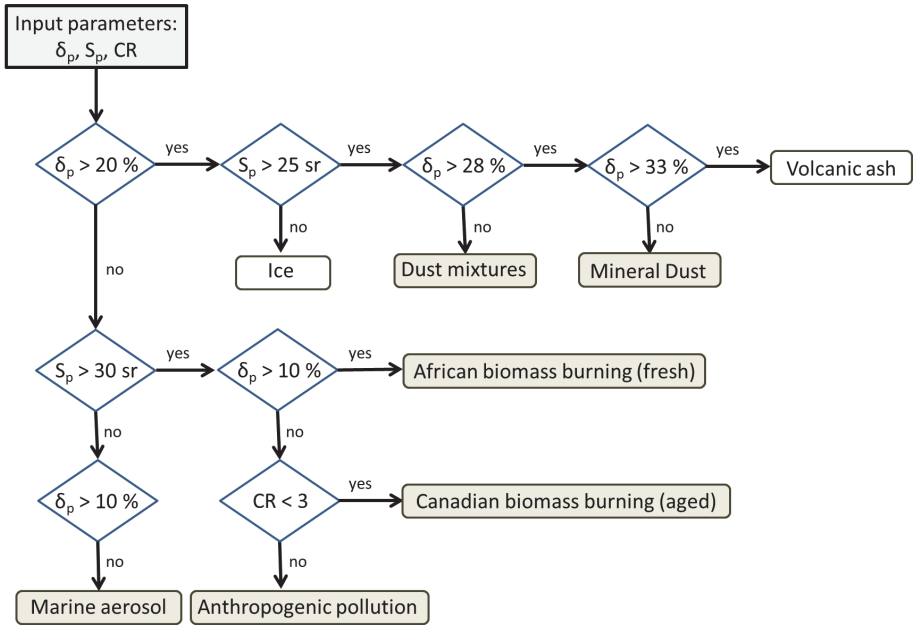

Fig. 8. Flowchart of the aerosol type classification based on three intensive lidar derived optical properties. Grey shaded aerosol types represent aerosol types characterized by DLR HSRL measurements, white shaded aerosol types are defined from literature information.

ACPD
12, 25983–26028, 2012

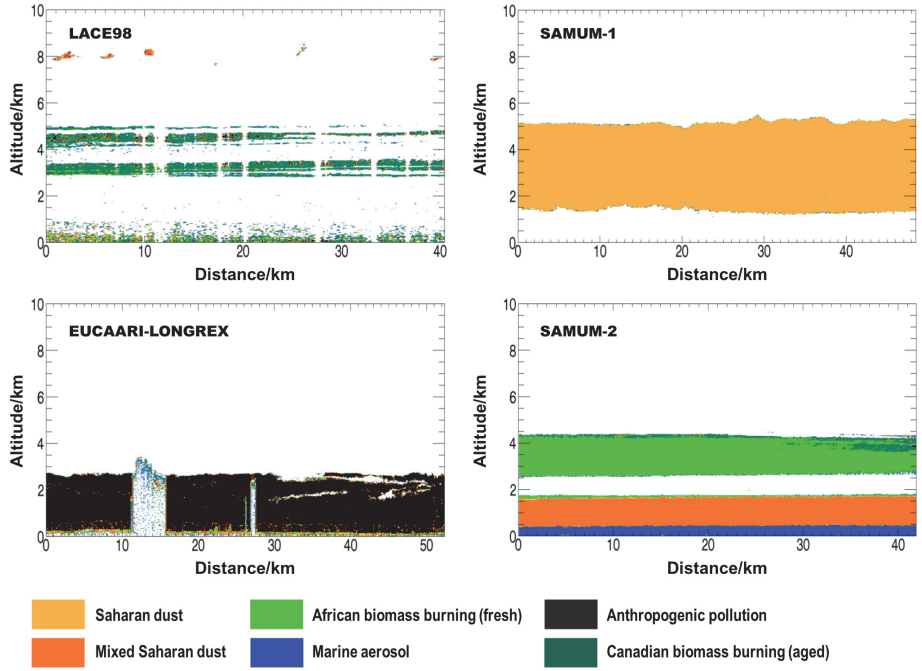

Fig. 9. Aerosol mask for the measurement examples shown in Fig. 4. The aerosol layers are color-coded corresponding to their aerosol type distinguished by intensive lidar optical properties as described in Fig. 8.

ACPD
12, 25983–26028, 2012

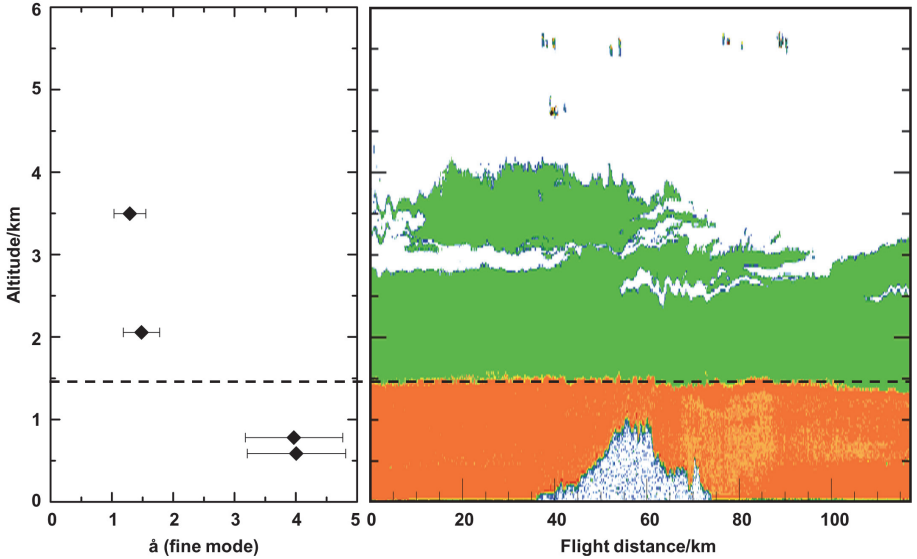

Fig. 10. Measurement example during SAMUM-2 on 25 January 2008. The left panel shows results of the in-situ measurements of the Angström exponent of absorption, the right panel shows the lidar signal, color-coded for the observed aerosol type (green for African biomass burning, orange for mixed Saharan dust).

ACPD
12, 25983–26028, 2012